2011 NDIA GROUND VEHICLE SYSTEMS ENGINEERING AND TECHNOLOGY SYMPOSIUM
MODELLING & SIMULATION, TESTING AND VALIDATION(MSTV) MINI-SYMPOSIUM
AUGUST 9-11 DEARBORN, MICHIGAN

Sensitivity Studies on Particle Emissions and Transport Around a Moving Vehicle

Xiaoling Tong
Center for Advanced Vehicle, Mississippi State University, MS
Edward A. Luke
Department of Computer Science, Mississippi State University, MS
Robert E. Smith
US Army TARDEC, Warren, MI

Abstract

The paper will provide representative simulations of particle transport around a vehicle in order to investigate some of the issues related to the accurate prediction of emission and transport of particles induced by a moving vehicle with a transverse blowing wind. Special treatments in boundary conditions and wall law function are discussed and applied to maintain the shape of atmospheric boundary layer wind velocity profile. For the vehicle, we adopt the geometry of a Nissan Pathfinder SUV to study the effects of vehicle emission and transport around a moving vehicle. We perform a set of simulations to better understand the modeling requirements for dust emissions including a sensitivity study to determine the modeling parameters that are most important for accurate modeling of dust generation and transport. In particular, we study the effects of location, size distribution, and initial velocity distributions of the modeled dust emissions on predicted downwind atmospheric dust distributions.

1 INTRODUCTION

The transport of dust in the air generated by vehicles traveling through a dusty terrain can have significant impact on many aspects of vehicle performance. Operationally, dust can be ingested by the engine and power train, increasing maintenance expense and reducing vehicle lifetime. In convoy types of operations, dust emissions can adversely effect visibility, particularly if dust accumulates on vehicle wind shields and mirrors. In commercial applications, the transport of particulates around a vehicle is of particular interest in determining vehicle soiling.

When a vehicle travels on an unpaved road, the forces of the rolling wheels impacted on the road surface crush large particles into smaller pieces and eject them into the air. The vertical pressure of the wheel on the ground causes the pulverization of surface material. Horizontal friction which sustains the vehicle velocity and acceleration of the vehicle further brings the particles on the surface of the tire. The slippage between the tire and the road lifts particles due to the shear force, and ejects them into the air due to centrifugal force. Saltation is another dust generation mechanism, which involves the bouncing of bigger particles on the road, and thus kicking smaller particles into the air. Fine particles can also entrained in the turbulent air behind the vehicle. Generally, bigger particles fall back to the ground surface more rapidly while smaller particles transfer with the air current. Some discussions on dust generation mechanisms can be found in the literature [1, 2]. There are many factors affect the generation of the dust, such as dust particle properties (size, density, stickiness, etc.), environment conditions

(wind speed,etc.), soil conditions (silt content, moisture level, etc) and vehicle features (vehicle velocity, weight, dimension, number of the wheels, etc.). There have been many research efforts in investigation of the relationship between the magnitude of dust emission and the above factors [3, 4, 5, 6], However, there is still no complete model that can accurately characterize and quantify this relationship due to the complexity and variability of the problem.

Most experimental work on dust emission induced by vehicles was targeted on environmental protection (pollution control) applications [6, 5, 7, 8, 9, 10], thus there is a lack of experimental data on dust concentration in the close vicinity of vehicles. Numerical work performed by a research group in George Mason University [2, 11] focused on a real-time simulation of dust behavior generated by moving vehicles. Since their purpose was to simulate the dust behavior in virtual environment for interactive graphic applications, and the computational time had to be fast enough to realize the true environment, the numerical models were over-simplified.

In this study, particle transport around a representative vehicle (Nissan Pathfound SUV) is simulated using Loci/CHEM code and its Lagrangian particle model. A fully developed transverse wind profile is imposed. In the following sections, development of atmospheric boundary layer (ABL) is discussed with details on boundary condition treatment and turbulence model. Then, numerical simulations on particle transport in the air induced by a moving vehicle will be presented, with the discussion of Lagrangian particle approach and preliminary results on sensitivity of the dust distribution.

2 DEVELOPMENT OF ATMOSPHERIC BOUNDARY LAYER

Since dust particles are transported and diffused in the air, it is necessary to accurately describe the atmospheric boundary layer. Because the simulation domain is normally much smaller compared to the scale of the terrain, it is not possible to obtain a fully developed ABL by applying a uniform flow at the domain boundaries. Thus, a prescribed ABL velocity profile is normally set at the inflow, and it is important that this profile maintains its shape along the fetch. Richard and Hoxey [12] have proposed a set of boundary conditions to ensure a homogeneous boundary layer. The standard logarithmic velocity profile with the consideration of surface roughness length is imposed on the inflow boundary. At the top boundary, a constant shear stress is applied to compensate the energy lost due to the shearing on the ground. In addition, the surface roughness has to be incorporated either in the boundary condition of viscous wall, or through a wall function which is based on boundary-layer theory for the computational cell immediately adjacent to the wall. We will start with describing the wall function with the consideration of the roughness height. The turbulence model adopted in this study, with the inclusion of wall roughness treatment will be presented. To evaluate the effectiveness of the boundary condition treatment, we will perform a simulation of flow over a flat surface with one kilometer in length to determine the model's ability to preserve the natural ABL.

2.1 Wall Function Boundary Condition

In order to save computational expense, a wall law function is often prescribed at the wall boundary. The typical boundary layer velocity profile consists of a thin sublayer at the bottom ($y^+ < 10$), a logarithmic profile for the $30 < y^+ < 1000$, and buffer layer in between. y^+ is the dimensionless distance to the wall defined as

$$y^+ = \frac{yu^\star}{\nu} \tag{1}$$

where $u^\star$ and ν are friction velocity and dynamic fluid viscosity respectively. There are several empirical relationships available for the velocity in a boundary layer that can be used to develop wall function boundary conditions. The formulation of Spalding [13] is adopted in this study, and it is a unified form valid for the log layer and sublayer as well as the transition region. This form is given by

$$y^+ = u^+ + e^{-\kappa B}[e^{\kappa u^+} - 1 - \kappa u^+ - \frac{(\kappa u^+)^2}{2} - \frac{(\kappa u^+)^3}{6}] \tag{2}$$

in which κ and B are dimensionless constants in the log layer profile ($\kappa = 0.41$), u^+ is defined as

$$u^+ = \frac{u}{u_\star} \tag{3}$$

For smooth wall, the constant B is approximately set to 5.2. For surfaces with average roughness height of k_s, the above wall law still holds. However, the additive constant, B is a function of k_s in the rough wall cases. Cebeci and Bradshaw [14] suggested the following correlation of Nikuradse's data [15] to evaluate the B:

$$B = \begin{cases} \left(-3.3 + \frac{1}{\kappa} ln\kappa_s^+\right) sin[0.4258(ln\kappa_s^+ - \\ 0.8111)] + 5.2, & 2.25 \leq \kappa_s^+ \geq 90 \\ \left(-3.3 + \frac{1}{\kappa} ln\kappa_s^+\right) + 5.2, & \kappa_s^+ > 90 \end{cases} \tag{4}$$

This correlation is implemented to compute the constant B if wall roughness is considered.

2.2 Baseline Turbulence Model (BSL)

There are several turbulence models implemented in the CHEM solver. Since the wall roughness treatment is only implemented in the Menter's Baseline model (BSL) and Wilcox (1998) [16] models, and BSL model is an modification of Wilcox (1998) model, we will only describe the BSL model in the following.

It is well known that two-equation eddy-viscosity *low-Reynolds-number* turbulence models are among the most widely used models for engineering applications today, and the $k-\epsilon$ model with damping functions near the wall is the most popular. However, the $k-\epsilon$ model often suffers from numerical stability problems due to disparate turbulent time scales. Another well-known two-equation turbulence model is the $k-\omega$ model, developed by Wilcox[17]. It has the advantage that it does not require damping functions in the viscous sublayer and that the equations are less stiff near the wall, therefore it is superior to $k-\epsilon$ model with regard to numerical stability. However, when applied to the free shear layers, it is found that there is a strong dependency of the results on the free stream value of ω[18, 19]. Menter created a new model, called baseline (BSL) model, by blending the $k-\epsilon$ and $k-\omega$ models[20]. It utilizes the $k-\omega$ model in the wall region and gradually switches to the $k-\epsilon$ model away from the wall. To achieve this, the $k-\epsilon$ model is first transformed into a $k-\omega$ formulation, and an additional cross diffusion term is added (another diffusion term associated with turbulent kinetic energy is neglected in the formulation under certain assumptions[16]). The original $k-\omega$ equations are then multiplied by a blending function F_{bsl}, the transformed $k-\epsilon$ equations are multiplied by $(1-F_{bsl})$, and then both are added together. The blending function F_{bsl} is designed so that it is unity at the wall, and gradually approaches zero away from the wall. Note that the $k-\omega$ model can be easily obtained by setting $F_{bsl}=1$ identically.

The defining equations for the BSL model are written as:

Kinematic Eddy Viscosity:

$$\nu_t = k/\omega, \tag{5}$$

where ν_t is the turbulent viscosity, k is the turbulence kinetic energy, and ω represents the dissipation per unit turbulence kinetic energy.

Turbulent Stress Tensor:

$$\begin{aligned} \tau_{ij}^{'} &= \mu_t\left(\frac{\partial u_i}{\partial x_j}+\frac{\partial u_j}{\partial x_i}\right)-\frac{2}{3}\left(\mu_t\nabla\cdot\tilde{u}+\rho k\right)\delta_{ij}, \\ i &= 1,2,3, \quad j=1,2,3, \end{aligned}$$

Turbulent Kinetic Energy Equation:

$$\rho\frac{Dk}{Dt}=\tau_{ij}^{'}\frac{\partial u_i}{\partial x_j}-\beta^{\star}\rho\omega k+\frac{\partial}{\partial x_j}\Big[(\mu+\mu_t\sigma_k)\frac{\partial k}{\partial x_j}\Big], \tag{6}$$

Turbulent Dissipation Equation:

$$\begin{aligned} \rho\frac{D\omega}{Dt} &= \frac{\gamma}{\nu_t}\tau_{ij}^{'}\frac{\partial u_i}{\partial x_j}-\beta\rho\omega^2 \\ &+ \frac{\partial}{\partial x_j}\Big[(\mu+\mu_t\sigma_\omega)\frac{\partial\omega}{\partial x_j}\Big] \\ &+ 2(1-F_{bsl})\rho\sigma_{\omega 2}\frac{1}{\omega}\frac{\partial k}{\partial x_j}\frac{\partial\omega}{\partial x_j}. \end{aligned}$$

Closure Coefficients:

All the constants ϕ of the model are computed by blending the appropriate $k-\omega$ and $k-\epsilon$ constants, as follows:

$$\phi = F_{bsl}\phi_1+(1-F_{bsl})\phi_2, \tag{7}$$

where the constants ϕ_1 ($k-\omega$) are used are provided by Menter[20]

The blending function F_{bsl} is defined as follows:

$$F_{bsl}=tanh(arg_{bsl}^4), \tag{8}$$

where

$$arg_{bsl}=\min\Big[\max\Big(\frac{\sqrt{k}}{0.09\omega y},\frac{500\nu}{y^2\omega}\Big),\frac{4\rho\sigma_{\omega 2}k}{CD_{k\omega}y^2}\Big], \tag{9}$$

and y is the distance to the closest point away from the wall surface. In the above, $CD_{k\omega}$ is defined as:

$$CD_{k\omega}=\max\Big(2\rho\sigma_{\omega 2}\frac{1}{\omega}\frac{\partial k}{\partial x_j}\frac{\partial\omega}{\partial x_j},10^{-20}\Big). \tag{10}$$

The boundary conditions for k and ω at a solid wall are:

$$k=0, \quad \omega=10\frac{6\nu}{\beta_1(\triangle y_1)^2}, \tag{11}$$

where $\triangle y_1$ is the distance from the first cell center to the solid wall. For rough walls, the user-specified equivalent roughness height (k_s) is used to compute the solid wall value of ω from:

$$\omega=\frac{u_\tau^2}{\nu}S_R \tag{12}$$

where

$$S_R=\begin{cases}\left(\frac{200}{k_s^+}\right)^2, & k_s^+\le 5 \\ \frac{100}{k_s^+}+\left[\left(\frac{200}{k_s^+}\right)^2-\frac{100}{k_s^+}\right]e^{5-k_s^+}, & k_s^+>5\end{cases} \tag{13}$$

A surface is considered to be hydraulically smooth[1] when $k_s^+=u_\tau k_s/\nu<5$. A slightly rough wall boundary condition for ω can be derived by combining Eqs. (12) and (13) and to obtain[21]:

$$\omega=\frac{40000\nu}{k_s^2}, \tag{14}$$

in which k_s must be chosen to ensure that $k_s^+<5$.

[1] A hydraulically smooth surface is one in which the roughness height is smaller than the laminar sublayer.

2.3 Inflow and Top Boundary Conditions

To test our ability to simulate the ABL we adopted Richards and Hoxey's [12] inflow and top boundary conditions in our study since some aspects of their work have become a standard in computational wind engineering in order to sustain the ABL velocity profile. Based on the $k-\epsilon$ turbulence model, Richards and Hoxey suggested the profiles for velocity, turbulent kinetic energy and turbulent dissipation which satisfy the the $k-\epsilon$ model. The profile functions are written as

$$u = \frac{u_\star}{\kappa} ln\left(\frac{y+y_0}{y_0}\right), \tag{15}$$

$$k = \frac{u_\star^2}{\sqrt{C_\mu}}, \tag{16}$$

$$\epsilon = \frac{u_\star^3}{\kappa(y+y_0)} \tag{17}$$

where C_μ is a constant in $k-\epsilon$ model, equal to 0.09. Note that y_0 is the surface roughness length which is different from surface roughness height, k_s. There are numerous work on the relationship between k_s and y_0 [22](Hargreaves). If the eq.(15) is rewritten in the form of

$$u^+ = \frac{1}{\kappa} ln(y^+) + B \tag{18}$$

and is related to the formulation of the constant considering the roughness, eq.(4), we have $k_s \approx 30y_0$ and $B = -14.9$ in the current study.

The profiles of velocity, turbulent kinetic energy and turbulent dissipation represented through eq.(15) to (17) are imposed in the inflow. At the top of computational domain, a constant shear stress of $\rho u_\star^2$ is applied, as proposed by Richard and Hoxey, to maintain the energy balance.

2.4 Results on Boundary Layer on a Flat Plate

Air with far field temperature of $293K$ and pressure of $1atm$ flowing over a flat plate is carried out to test the homogeneity of velocity field in the flow direction. In our test case, we use the same prescribed inflow velocity profile as in Richards and Hoxey's [12] work. Thus, the friction velocity ($u_\star$) and the roughness length (y_0) in the eq.(15) are set to be $0.6m/s$ and $0.01m$ respectively, which were obtained by fitting the measured velocity data. The ground roughness height, k_s is set to $0.3m$ according to the relationship $k_s \approx 30y_0$, which leads to $k_s^+ = 12,000$. Roughness length (y_0) of $0.01m$ corresponds to the terrain condition of a lawn. For a level desert, y_0 is on the order of $0.001m$. Wilcox (1998) turbulence model [16] is used in this simulation since we found that Wilcox (1998) model converges better that BSL model for roughness height larger than $0.1m$. The wall law boundary condition is applied on the ground with y^+ equal to 150 at the first grid point away from the wall. The computational domain is $1km \times 0.5km$ in flow and vertical direction respectively.

The development of boundary layer along the plate is shown in figure 1. At first sight, it seems that the velocity profile maintains itself well along the domain. However, by zooming into the bottom of $10m$ of boundary layer, the discrepancy between the original inflow profile and downstream profile becomes apparent, as shown in figure 2. Figure 2 also includes the results without the roughness treatment in the wall function and shear stress application at the top. It is clear that the velocity profile maintains a much closer shape to the prescribed inflow profile if the roughness height is considered in the wall function and the shear stress is imposed at the top. There are a few possible reasons that can be contributed to the non-sustainability of the ABL even with Richards and Hoxey treatments. First, Richards and Hoxey model was based on $k-\epsilon$ model, while $k-\omega$ model is adopted to compute the turbulence in this study, which could cause some non-consistency regarding the model parameters. Second, there is difference between the prescribed friction velocity and actual friction velocity calculated from the code, as depicted in figure 3. Lower friction velocity results in the larger flow speed at the bottom of boundary layer, which is seen in the figure 2. The parameter, B, in the wall function is based on the prescribed friction velocity, and remained constant during the development of the boundary layer. The iterative calculation between computed friction velocity and the corresponding parameter, B in the wall function is proposed to eliminate the difference between the targeted and real friction velocity. Maintaining ABL profile is not a trivial problem, and more effort will be carried on in the future research. In the current application where computational domain is much smaller than $1km$, the sustainability of the ABL is satisfactory.

3 PARTICLE TRANSPORT IN THE AIR INDUCED BY A MOVING SUV

In this study, we have performed a number of representative simulations of particle transport around a representative vehicle in order to investigate some of the issues related to predicting emissions and transport of particles from a vehicle traveling with a transverse wind. For these simulations we utilize the Loci/CHEM code and its Lagrangian particle transport model. For the vehicle we adapted the geometry of a Nissan Pathfinder SUV that was previously used in blast studies in the SIMBRS WD19 task. A viscous mesh was generated on this SUV using the SolidMesh/AFLR3 software developed at Mis-

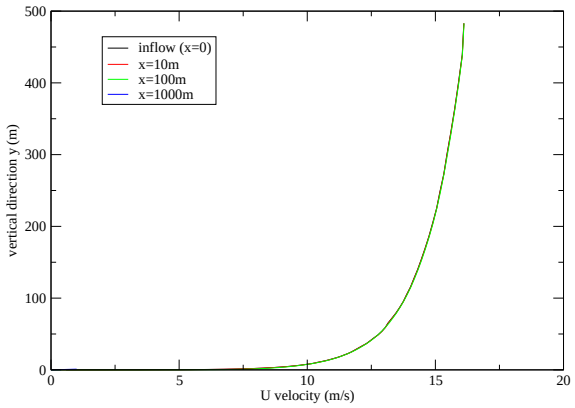

Figure 1: X-component velocity distribution in the vertical direction along the flat plate

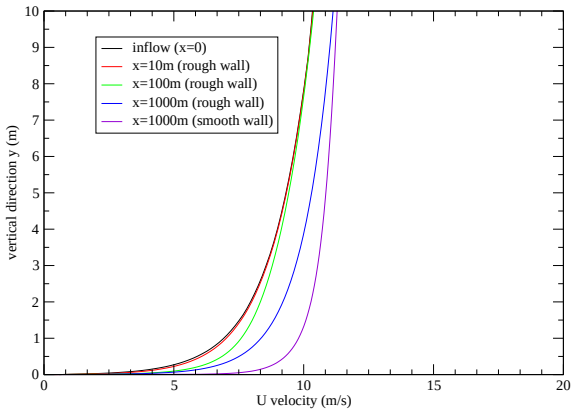

Figure 2: X-component velocity distribution in the vertical direction along the flat plate in the bottom $10m$ of boundary layer

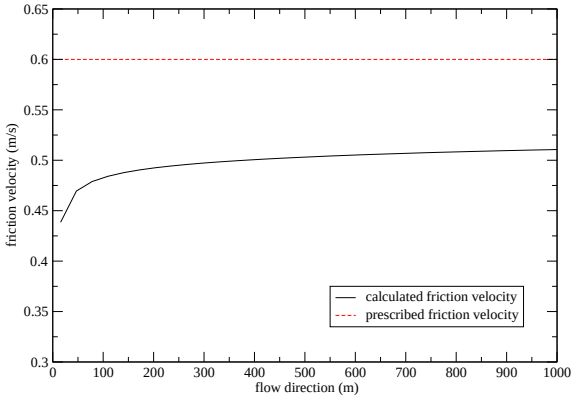

Figure 3: Comparison of prescribed friction velocity and the computed one

sissippi State. The final mesh was about 15 million cells. Cases were run on 48 processors of our cluster with turn around times on the order of 1-2 hours. The Lagrangian particle model, provided by a scalable parallel implementation using the Loci framework, is described in the following section.

3.1 Lagrangian Particle Approach

The governing equations Eqns. (19-20) for the particle movements were derived using the Basset-Boussinesq-Oseen (BBO) assumption that the density of the particle is much larger than that of the fluid and particle size is small compared to turbulence integral length scale, and that the effect of shear on particle motion is negligible:

$$\frac{dx_p}{dt} = u_p \tag{19}$$

$$\frac{du_p}{dt} = D_p(u - u_p) + F_v \tag{20}$$

where u_p is the particle velocity, and u is the gas-phase velocity interpolated to the particle location x_p. F_v is the body force which includes the gravity. Only momentum coupling is considered in the current study. The drag force on a solid particle is modeled using a drag-coefficient,

$$D_p = \frac{3}{4} C_d \frac{\rho}{\rho_p} \frac{|u - u_p|}{d_p} \tag{21}$$

where ρ and ρ_p are the density of fluid and the particle respectively, d_p is the particle diameter and C_d is obtained from the nonlinear correlation [23]:

$$C_d = \frac{24}{Re_p}(1 + aRe_p^b) \tag{22}$$

where $Re_p = d_p|u - u_p|/\mu$ is the particle Reynolds number. The constants $a = 0.15$, $b = 0.687$ are used to get the drag-coefficient.

The Lagrangian particle implementation uses an implicit backward differentiation scheme to support stiff source terms. The scheme is expressed in a generic form as:

$$x_p^{n+1} + \sum_{i=1}^{s} \alpha_i x_p^{n+1-i} = \Delta t \beta u_p^{n+1} \tag{23}$$

$$\begin{aligned} u_p^{n+1} + \sum_{i=1}^{s} \alpha_i u_p^{n+1-i} &= \Delta t \beta D_p (u^{n+1} - u_p^{n+1}) \\ &+ \Delta t \beta F_v^{n+1} \end{aligned}$$

where s is the total number of the multi-step scheme, Δt is the time step, and coefficients for the second order scheme used in current implementations are: $\alpha_1 = -\frac{4}{3}$,$\alpha_2 = -\frac{1}{3}$, and $\beta = -\frac{2}{3}$.

The injection of Lagrangian particles from the injection surface is needed to be handled in a more realistic way in the Lagrangian approach. The size and location of each injected particle is random. Some possible particle size distribution functions are the logarithmic normal distribution formulated as

$$Pr(d) = [1/\sqrt{(}2\pi)\sigma d]exp\{-(1/2\sigma^2)[ln(d/d_{med})]^2\}$$

given the median particle diameter d_{med} and a standard deviation σ, and the skewed logarithmic distribution:

$$\begin{aligned} Pr(d) &= [1-(d/d_{max})^2][1-(d_{min}/d)^2] \\ &\times \quad exp\{-(1/2\sigma^2)[ln(d)-\beta]^2\} \end{aligned}$$

where β is computed as

$$\beta = ln(d_{peak}) + \frac{2\sigma^2}{(d_{max}/d_{peak})^2 - 1}$$

given peak,minimum, and maximum particle diameter d_{peak}, d_{min}, d_{max}, respectively, and a standard deviation σ.

Since the flow field information is needed at the particle location during the Lagrangian particle equation integration process, it is necessary to find in which control volume the particle resides. Thus, the particle search and location schemes and interpolation schemes are implemented.

The purpose of the algorithm is to determine if a particle exists in a given control volume with arbitrary shape [24, 25, 26, 27, 28]. For the CHEM particle simulation we use the projection approach as utilized by Apte *et al*[28]. To enhance robustness, we mark particles that have an extended path length and track the cells through which they pass. Within any single time step, we do not allow a particle to pass through the same cell twice while searching for its containing cell. This produces a robust geometric searching algorithm for locating a particle within the cell of arbitrary polyhedral unstructured meshes.

The flow properties are interpolated using the limited cell reconstructions from the fluid phase simulations. This provides a spatially second order interpolation method.

3.2 Results on Particle Transport

For the simulation of particle generation and transport we consider an SUV type vehicle traveling with 13.5m/s (about 30mph) uniform forward velocity with a cross wind of 6.75 m/s (about 15mph). The wind is simulated either as a uniform flow or an ABL with a velocity of 6.75m/s at one meter height using a surface friction velocity of $u_\star = 0.6m/s$ and roughness length of $y_0 = 0.01m$. The rubber part of the tire is prescribed a rotational velocity 348.42 rpm which is consistent with a forward velocity of 13.5m/s. The rotation of the spokes of the hub is not considered in this model.

Particles are emitted using a tri-mode particle distribution with particle mean diameters of $2.5\mu m$, $10\mu m$ and $100\mu m$ with a mass distribution of 10%, 80%, and 10% respectively. Each size group is emitted with a log-normal distribution of its mean particle diameter with a variance of $\sigma = 0.25$. Particles have a material density of quartz which is 2648 kg/m^3 and are injected from the tires at a mass flux of 0.1 kg/m^2 with a speed of 95% of the wheel velocity for the cases where tires were treated as the source and a similar mass flux from a small patch under the tires at a fixed upward velocity of 4m/s in one case. The BSL turbulence model was employed in all simulations. The effects of turbulence diffusion on the particles is not considered in this simulation as we will need to implement a turbulence-particle coupling term. We will likely use a first order continuous Markov model to model turbulent velocity fluctuations in future simulations.

Our first simulation considers a prescribed uniform flow for the wind with particles emitted from the tire surfaces. A side, back, and top view of this simulation is shown in figures 4, 5, and 6 with the vehicle surface colored by computed pressures. Particles are colored by a gray scale indicating particle diameter with larger particles being darker in color. These view show that the particle model qualitatively behaves as expected, with particles being entrained in the wake flow of the vehicle much as one would expect. We then compare changing the location of particle emissions from the tires to the ground in a small region around the tire. A front view of the particle distributions for the uniform flow showing the tire emission is illustrated in figure 7 while the results from the ground emission is shown in figure 8. Although the ground emissions result in a particulate cloud that is hangs closer to the ground, the two cases are surprisingly similar suggesting that there is only modest sensitivity to the means in which particles are injected into the simulation. Finally, we consider the effects of the atmospheric boundary layer on the simulation (this time with emissions from the tires) and find that there are significant differences in the plume shape. We expect that these differences will become more significant as we add turbulent effects to the particle coupling as the atmospheric boundary layer will significantly increase particle scattering behind the vehicle.

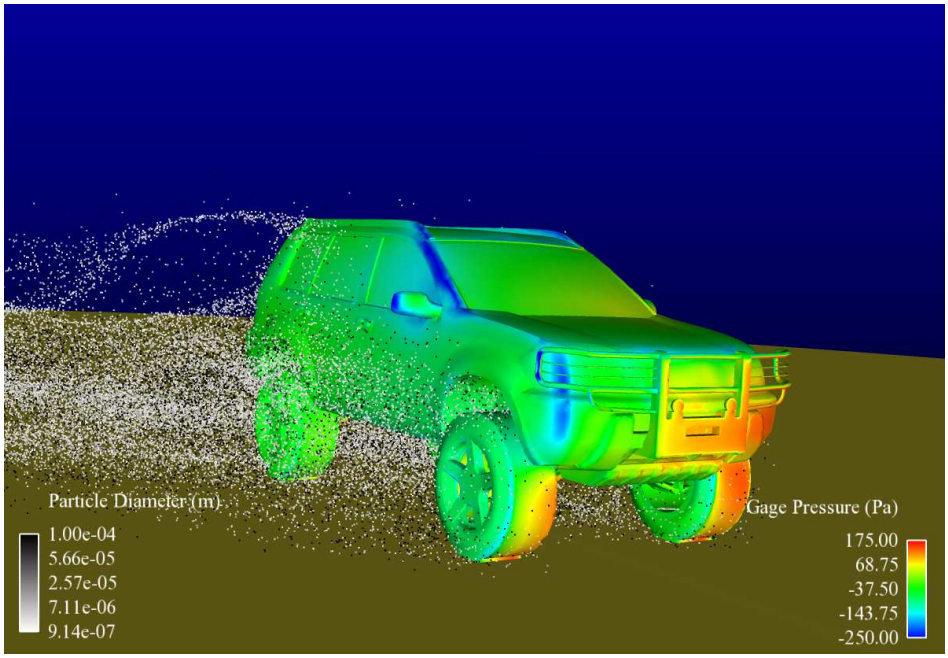

Figure 4: Side view of particle distribution for tire emission using uniform wind model. Vehicle colored by pressure.

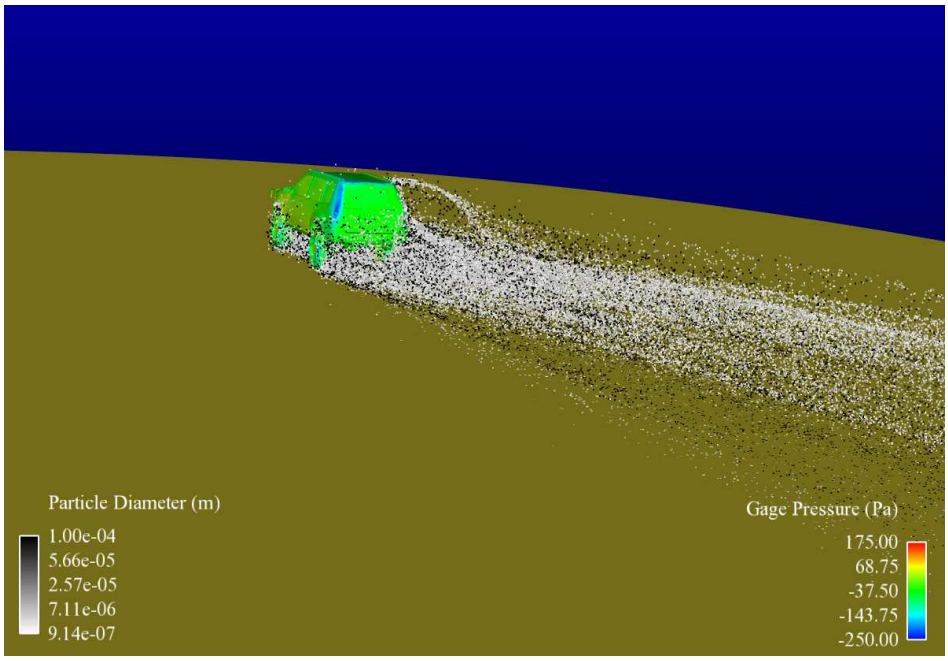

Figure 5: Back view of particle distribution for tire emission using uniform wind model. Vehicle colored by pressure.

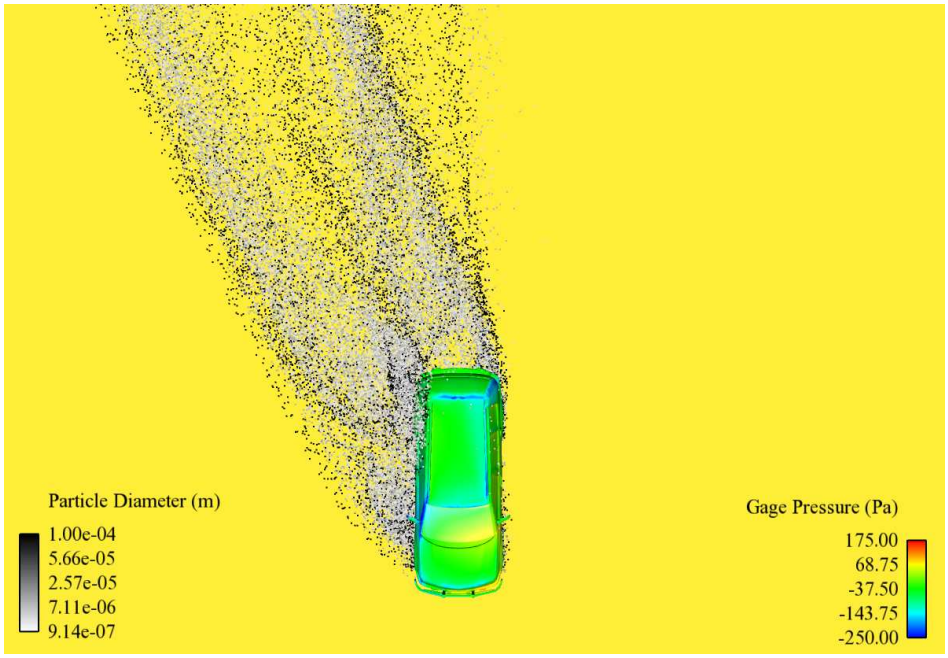

Figure 6: Top view of particle distribution for tire emissions using uniform wind model. Vehicle colored by pressure.

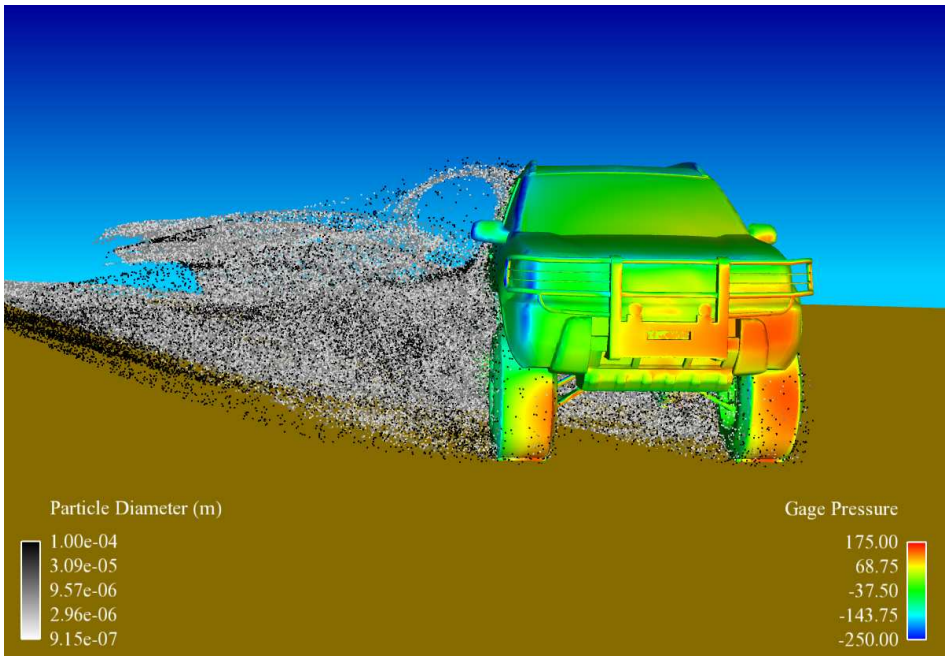

Figure 7: Front view of particle distribution for tire emissions using uniform wind model. Vehicle colored by pressure.

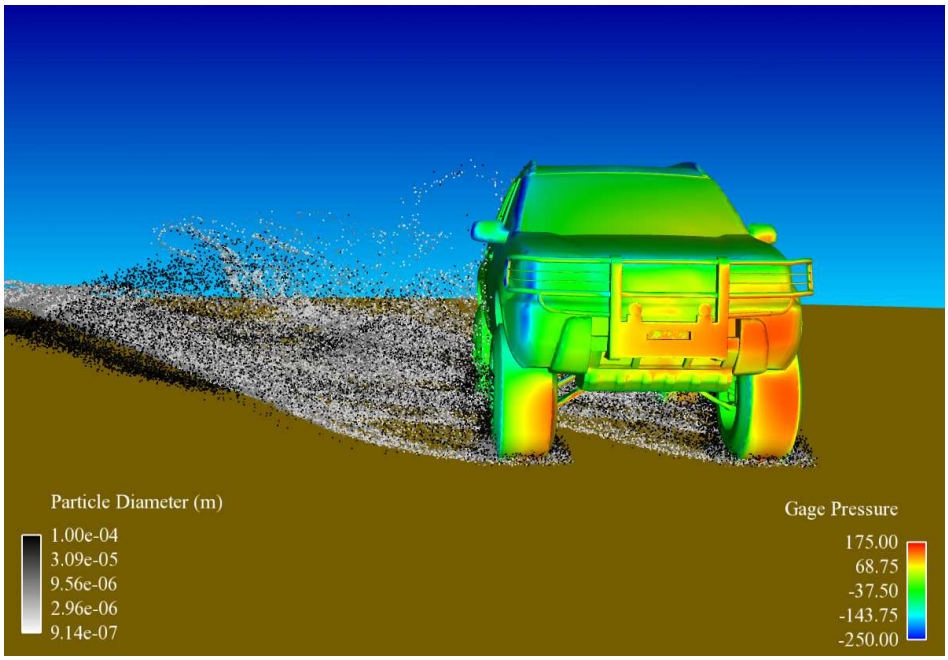

Figure 8: Front view of particle distribution for ground emissions using uniform wind model. Vehicle colored by pressure.

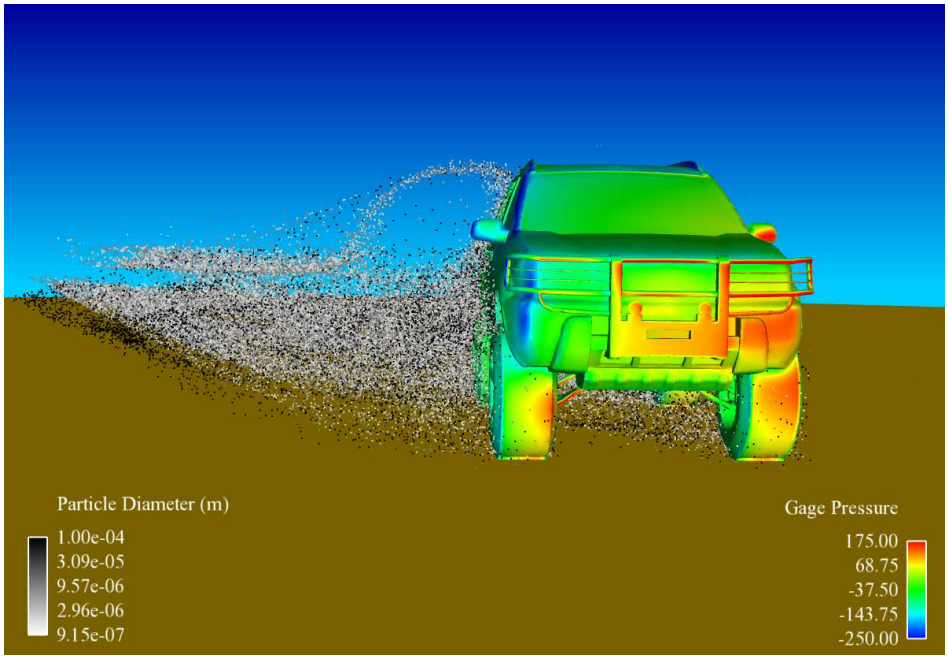

Figure 9: Front view of particle distribution for tire emissions using atmospheric boundary layer wind model. Vehicle colored by pressure.

Disclaimer

Reference herein to any specific commercial company, product, process, or service by trade name, trademark, manufacturer, or otherwise, does not necessarily constitute or imply its endorsement, recommendation, or favoring by the United States Government or the Department of the Army (DoA). The opinions of the authors expressed herein do not necessarily state or reflect those of the United States Government or the DoA, and shall not be used for advertising or product endorsement purposes.

References

[1] M. Succarieh. Control of dust emissions from unpaved roads. Technical report, University of Alaska, May 1992. Prepared for Alaska Cooperative Transportation and Public Facilities Research Program.

[2] J. Chen, X. Fu, and E. Wegman. Real-time simulation of dust behavior generated by a fast traveling vehicle. *ACM Transactions on Modeling and Computer Simulation*, 9(2):81–104, 1999.

[3] C. Cowherd. Sandblaster 2 support of see-through technologies for particulate brownout. Technical report, 2007. Task 5 Final Technique Report, MRI Project No. 110565.

[4] US Environmental Protection Agency, Research Triangle Park, NC. *AP-42, Miscellaneous Source Chapter 13*, fifth ed. edition, 2003.

[5] J. Gillies, V. Etyemezian, H. Kuhns, H. Mmsmuller, J. Engelbrecht, J. King, S. Uppapalli, G. Nikolic, J. McAlpine, D. Zhu, M. Skiba, and D. Gillette. Particulate matter emissions factors for dust from unique military activities. Technical report, DRI, 2010. SERDP Project SI-1399.

[6] J. Gillies, V. Etyemezian, H. Kuhns, D. Nikolic, and D. Gillette. Effect of vehicle characteristic on unpaved road dust emissions. *Atmospheric Environment*, 39:2341–2347, 2005.

[7] J. Veranth, E. Pardyjak, and G. Seshadri. Vehicle-generated fugitive dust transport: analytic models and field study. *Atmospheric Environment*, 2003.

[8] H. Kuhns, V. Etyemezian, and P. Shinbein. Relating road dust emissions surrogates to average daily traffic and vehicle speed in las vegas, nevada. Technical report, DRI and Clark County Comprehensive Planing, not know.

[9] V. Etyemezian, H. Kuhns, J. Gilles, M. Green, M. Pitchford, and J. Watson. Vehicle-based road dust emission measurement: I–methods and calibration. *Atmospheric Environment*, pages 4559–4571, 2003.

[10] V. Etyemezian, H. Kuhns, J. Gilles, J. Chow, K. Hendrickson, M. McGown, and M. Pitchford. Vehicle-based road dust emission measurement: Iii–effect of speed, traffic volume, location, and season on pm_{10} road dust emissions in the treasure valley, id. *Atmsopheric Environment*, pages 4583–4593, 2003.

[11] J. Chen, E. Wegman, and J. Wang. Animation of dust behaviors in a networked virtual environment. This article is found using google. No information on the year and where published.

[12] P. Richards and R. Hoxey. Appropriate boundary conditions for computational wind engineering models using the $k-\epsilon$ turbulence model. *Journal of Wind Engineering and Industrial Aerodynamics*, 1993.

[13] D. B. Spalding. A single formular for the law of the wall. *Transactions of the ASME, Series E: Journal of Applied Mechanics*, 5(17), 1961.

[14] T. Cebeci and P. Bradshaw. *Momentum Transfer in Boundary Layers*. Hemisphere Publishing, 1977.

[15] J. Nikuradse. Laws of flow in rough pipes. Technical Report Tech. Rep. NACA TM 1292, NACA, 1950.

[16] D. C. Wilcox. *Turbulence Modeling for CFD*. DCW Industries, 1998.

[17] D. C. Wilcox. Reassessment of the scale-determining equation for advanced turbulence models. *AIAA Journal*, 26(11):1299–1310, 1988.

[18] D. C. Wilcox. A half century review of the $k-\omega$ model. Technical report, AIAA, 1991. AIAA 91-1784.

[19] F. R. Menter. Influence of freestream values on $k-\omega$ turbulence model predictions. *AIAA Journal*, 30(6):1657–1659, June 1992.

[20] F. R. Menter. Two-equation eddy-viscosity turbulence models for engineering applications. *AIAA Journal*, 32(8):1598–1605, August 1994.

[21] D. C. Wilcox. Formulation of the $k-\omega$ turbulence model revisited. *AIAA J.*, 46(11):2823–2838, 2008.

[22] J. Franke, C. Hirsch, A. G. Jensen, H. W. Schatzmann, P. S. Westbury, S. D. Miles, J. A. Wisse, and N. G. Wright. Recommendations on the use of cfd in wind engineering. In J.P.A.J van Beeck, editor, *Proceedings of the International Conference Urban*

Wind Engineering and Building Aerodynamics. von Karman Institute, 2004.

[23] M. Sommerfeld C. Crowe and Y. Tsuji. *Multiphase flows with droplets and particles*. CRC Press, 1998.

[24] R. Lohner and J. Ambrosiano. A vectorized particle tracer for unstructured grids. *Journal of Computational Physics*, 91:22–31, 1990.

[25] T. Westermann. Localization schemes in 2d boundary-fitted grids. *Journal of Computational Physics*, 101:307–313, 1992.

[26] R. Lohner. Robust, vectorized search algorithms for interpolation on unstructured grids. *Journal of Computational Physics*, 118:380–387, 1995.

[27] A. Allievi and R. Bermejo. A generalized particle search-locate algorithm for arbitrary grids. *Journal of Computational Physics*, 132:157–166, 1997.

[28] P. Moin S. V. Apte, K. Mahesh and J. C. Oefelein. Large-eddy simulation of swirling particle-laden flows in a coaxial-jet combustor. *International Journal of Multiphase Flow*, 29:1311–1331, 2003.